A Benchmark Study of Burning Rate of Selected Thermites through an Original Gasless Theoretical Model

Sarah Brotman, Mehdi Djafari Rouhani, Samuel Charlot, Alain Estève, Carole Rossi

applied sciences

MDPI

Article

A Benchmark Study of Burning Rate of Selected Thermites through an Original Gasless Theoretical Model

Sarah Brotman, Mehdi Djafari Rouhani, Samuel Charlot, Alain Estève * and Carole Rossi *

LAAS-CNRS, University of Toulouse, 7 Avenue du Colonel Roche, 31400 Toulouse, France; sbrotman@laas.fr (S.B.); djafari@laas.fr (M.D.R.); scharlot@laas.fr (S.C.)

* Correspondence: aesteve@laas.fr (A.E.); rossi@laas.fr (C.R.); Tel.: +33-5-61-33-63-53 (C.R.)

Abstract: This paper describes a kinetic model dedicated to thermite nanopowder combustion, in which core equations are based on condensed phase mechanisms only. We explore all combinations of fuels/oxidizers, namely Al, Zr, B/CuO, Fe_2O_3, WO_3, and Pb_3O_4, with 60 % of the theoretical maximum density packing, at which condensed phase mechanisms govern the reaction. Aluminothermites offer the best performances, with initiation delays in the range of a few tens of microseconds, and faster burn rates (60 cm s^{-1} for CuO). B and Zr based thermites are primarily limited by diffusion characteristics in their oxides that are more stringent than the common Al_2O_3 barrier layer. Combination of a poor thermal conductivity and efficient oxygen diffusion towards the fuel allows rapid initiation, while thermal conductivity is essential to increase the burn rate, as evidenced from iron oxide giving the fastest burn rates of all B- and Zr-based thermites (16 and 32 cm·s^{-1}, respectively) despite poor mass transport properties in the condensed phase; almost at the level of Al/CuO (41 versus 61 cm·s^{-1}). Finally, formulations of the effective thermal conduction coefficient are provided, from pure bulk, to nanoparticular structured material, giving light to the effects of the microstructure and its size distribution on thermite performances.

Keywords: energetic materials; nanothermite powders; modelling; burn rate; initiation

Citation: Brotman, S.; Djafari Rouhani, M.; Charlot, S.; Estève, A.; Rossi, C. A Benchmark Study of Burning Rate of Selected Thermites through an Original Gasless Theoretical Model. *Appl. Sci.* **2021**, *11*, 6553. https://doi.org/10.3390/app11146553

Academic Editors: Cristoph Pauly and Karsten Woll

Received: 9 June 2021
Accepted: 10 July 2021
Published: 16 July 2021

1. Introduction

Thermites in the form of mixed particles composed of a fuel, most commonly aluminum, and an oxidizer, such as iron, copper oxide, or molybdenum oxide [1–10], have attracted considerable attention due to their controllable versatility and high reaction enthalpies, making them good candidates for a number of applications including actuation [11,12], micropropulsion [13–17], heat sources for welding or joining [18,19], and, more recently, micro-initiation and environmentally clean primers [20–23]. In the last two decades, nano-sized particles have been widely studied due to their advances in reactivity, e.g., lower initiation temperature, lower initiation delay, and shortened kinetics of heat release, which was a necessary development to further improve the performances of the aforementioned applications, with the potential to dethrone other types of energetic compositions [24–27].

While nanosized particles were found to outperform their micron counterparts, the performance enhancements were below expectation, and, thus, the exact mechanisms by which these augmentations are accomplished remains debated [28–35]. In theory, mixed nanoparticles possess higher interfacial contact and a decrease in mass-transport lengths resulting in much wider reaction fronts. However, the loss of their nanostructures during the early stage of initiation due to sintering was experimentally observed, providing an explanation for the longer than expected burn times [5,36,37]. Prior to this, a debate in the community of thermite materials was focused on whether condensed phase rather than gas phase mechanisms were responsible for the different combustion regimes, e.g., initiation and combustion. Evidently, both mechanisms are expected to be present when considering

the level of heating and temperatures reached upon initiation and subsequent reaction propagation; yet, the balance between the two mechanisms, and the potential domination of one over the other in either stage of combustion is complex and difficult to ascertain. Indeed, this balance is shown to depend heavily on the overall nanostructure (dense vs. low compaction, open vs. closed architecture), as well as the method of initiation (very high vs. low heating rate, laser heating, ESD, etc.), and obviously, the chemical nature of the thermite ingredients [38,39].

In this respect, modelling, ranging from atomic to macroscale methodologies, is a useful tool to probe specific, if not the overall, aspects of the complex heterogeneous combustion that are still not fully understood. At the atomic scale, simulations that are governed by molecular dynamics and/or density functional theory (DFT) are mostly limited to a scope of basic mechanisms and early stages of initiation of the reaction due to limitations in system size and the long calculation time required for these types of simulated experiments [40–44]. At the other extreme, analytical models of macroscale systems are generally using rudimentary approximations of the chemical fundamentals governing the reaction of thermite materials [45–48]. Therefore, mesoscale models offer a good compromise through the inclusion of physico-chemical insights into the material properties and mechanisms (diffusion/reactions), making them more versatile and predictive for a wider range of materials and experimental conditions. Along this line, several models have been proposed to elucidate the importance of gas phase versus condensed phase mediated thermite reaction processes [39,49,50]. A recent publication proposed a pure condensed-phase model based on a spherical formulation of the Deal and Grove diffusion-reaction scheme [51] coupled to the heat equation. This approach included a wetting component allowing the exploration of the effect of a reactive sintering process as defined in References [5,52]. The model was first employed to quantify the effect of a condensed phase process on the initiation delay of an Al/CuO powder thermite under different heating rates, and the results were compared with the purely gas phase-mediated reaction approach of V. Baijot et al. [39,50,53]. In this way, condensed phase mechanisms (diffusion and reactions within the condensed matrix), can be opposed to gas phase processes, in addition to what other mechanisms such as mechanical rupture or advection are still to be evaluated and taken into considerations in modelling approaches of thermites. However, it was demonstrated that initiation can be reasonably estimated from exclusively condensed phase mechanisms with the following conditions: the nano to microsecond regime of initiation under very high heating rate (10^{11} K·s^{-1}) requires a pronounced amount of sintering to be obtained, while for medium range heating rate (10^{5} K·s^{-1}), the degree of sintering affects initiation to a much lesser extent.

Following this work dedicated to initiation via condensed phase mechanisms [39], one fundamental issue remains on the effects of these specific condensed phase mechanisms on propagation of the combustion front, which is the purpose of the present paper. We will discuss into great detail the respective role of thermal conductivity and the ability of oxygen to be transported towards the fuel and reaction enthalpy, by comparing initiation time and burn rate of a selection of different thermites. After detailing the theoretical approach, stoichiometric combinations of fuel (Al, B, and Zr) with oxidizers (CuO, Fe_2O_3, WO_3, and Pb_3O_4) will be considered within an axisymmetric, open-air system. We will also propose and evaluate different effective thermal conductivity expressions from which we will learn more about to which extent the nanostructure and mixture quality (presence of heat sinks, thermal insulating discontinuities, or size dispersed particles) affect combustion properties.

2. Methodology

2.1. System Model

The model is designed as an open system of a one-dimensional (1D) discretized chain of identical cells where each elemental cell is populated according to the theoretical maximum density percentage (%TMD) with N single fuel-oxidizer pairs (see Figure 1). %TMD is the ratio between the particles' volume and the total cell volume. Initiation is

obtained by the application of a power density at the first cell at the left extremity of the 1D system. The reaction front propagates from the left to the right side of the system shown in Figure 1.

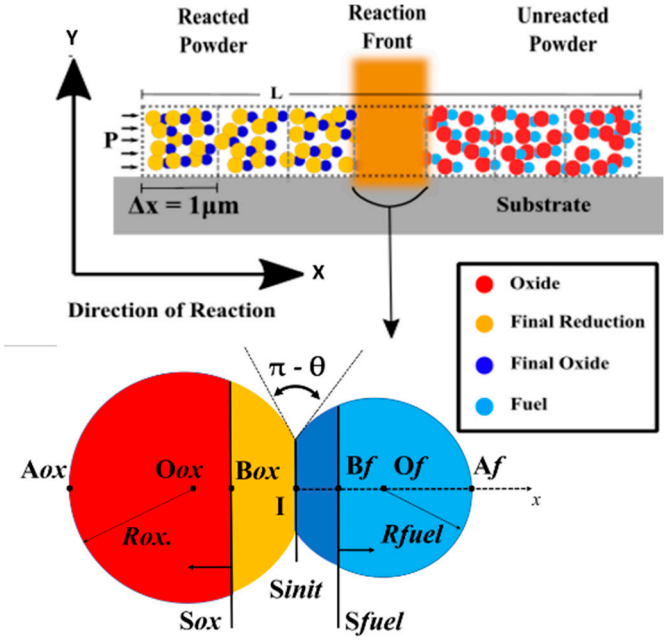

Figure 1. Geometry of the modelled thermite system and main model parameters: top figure, general view of the system, with the reaction front propagating from the left to the right. Lower figure, a magnified view of one fuel/oxidizer particle pair, with its multiple interfaces as the reaction propagates.

A contact angle θ fixed at 135° (see Figure 1, lower scheme) is chosen to represent the degree of coalescence (sintering) of the two adjacent spherical fuel and oxidizer nanoparticles before combustion starts. This value was observed for usual experimental conditions in Al/CuO nanopowders [38,52].

2.2. Diffusion/Reaction Model

At the nanoscale, the thermite reaction is simulated using a diffusion-reaction scheme, which allows the calculation of the combustion kinetics of the various species. The main assumption is that the chemistry driving the thermite combustion is restricted to a purely condensed phase process in which only oxygen is considered as a migrating species: oxygen diffuses through the growing oxide layer (i.e., the product of reaction) to react spontaneously upon reaching the fuel. It is, thus, assumed that the starting reactants and reaction products are in the solid state and exhibit thermal homogeneity. As shown in Figure 1, upon oxygen diffusion from the oxidizer and further reaction at the growing oxide interaction (i.e., oxide reaction product) with the fuel, the initial interface layer between the fuel and oxidizer (associated S_{init}, Figure 1) propagates throughout the fuel particle (associated surface noted S_{fuel}, Figure 1). Similarly, a front of reduction propagates into the oxidizer particle (noted S_{ox}, Figure 1).

The one-dimensional oxygen flux (noted ϕ) along the x direction obeys the general form:

$$\phi(x) = -\mathrm{D} \times S(x) \times \frac{dC(x)}{dx} \quad (1)$$

where D and $C(x)$ are the temperature dependent diffusion coefficient and concentration (in mol.m^{-3}) of the oxygen species, respectively. $S(x)$ is the surface area of the interface,

assumed to be flat, at a distance x from the center of a sphere of radius R, either oxidizer or fuel as shown in Figure 1, expressed as:

$$S(x) = \pi\left(\mathrm{R}^2 - x^2\right) \tag{2}$$

Note that ϕ represents here the total flux and not the flux density, as generally used in 1D problems with a constant surface. In the Deal and Grove scheme [51], the flux is considered as constant between S_{fuel} and S_{ox}. Therefore, Equation (1) can be integrated to express the oxygen concentration C at the various interfaces. The integral of 1/S(x) is a logarithmic function and we found:

$$\mathrm{C(x)} = -(\phi/2\pi \mathrm{DR} \times \ln((\mathrm{R}+\mathrm{x})/(\mathrm{R}-\mathrm{x})) + Constant \tag{3}$$

Applying this relation in the two regions that include, respectively, IB_{ox} and IB_f segments (see Figure 1), i.e., at point I, B_{ox}, and B_f, summing them and imposing $\mathrm{C}(B_{ox})$ = Cs, Cs being the solubility limit in the reduced oxide, we found:

$$\mathrm{C}\left(B_f\right) /2\pi \left[\frac{1}{R_{ox}D_{ox}}\ln\left(\frac{(R_{ox}+IO_{ox})(R_{ox}-O_{ox}B_{ox})}{(R_{ox}-IO_{ox})(R_{ox}+O_{ox}B_{ox}}\right) + \frac{1}{R_fD_f}\ln\left(\frac{(R_f+IO_f)(R_f-O_fB_f)}{(R_f-IO_f)(R_f+O_fB_f}\right)\right] \tag{4}$$

Note that D_f is the diffusion coefficient of oxygen in the oxidized fuel, as for instance Al_2O_3 when dealing with aluminum-based thermites. In addition, at the reactive interface between the growing oxide and the fuel, the oxygen flux oxidizes Al at a rate v, such that:

$$\phi = v\,\pi\,\mathrm{C}\left(B_f\right)\left[R_f^2 - \left(IB_f\right)^2\right] \tag{5}$$

Combining Equations (4) and (5), we found the oxygen flux as a function of C_s, the solubility limit of oxygen in the metal oxide oxidizer, whatever its reduction degree, such as Cu_2O or pure Cu, when considering CuO oxidizer. Then, the oxygen flux allows the calculation of the oxidizer and the fuel interface progression:

$$\frac{dIB_{ox}}{dt} = \phi\Omega_{ox}/\,\pi\left[R_{ox}^2 - (IB_{ox})^2\right]$$
$$\frac{dIB_f}{dt} = \phi\Omega_f/\,\pi\left[R_f^2 - \left(IB_f\right)^2\right] \tag{6}$$

where Ω_{ox} and Ω_f are molar volumes of the oxidizer and the oxidized fuel, respectively. Note also that the flux is constant across various interfaces, but is not constant over time.

At the macroscopic scale, within each unit cell along the X direction (see Figure 1), this diffusion reaction scheme is coupled to a heat equation (through $\phi's$), that enables mapping of the system temperature. The heat equation has the standard form:

$$C_V\frac{dT}{dt} = P + \phi(X)q + \sum h_j\delta\left(T - T_j\right) + \lambda\frac{d^2T}{dX^2} - \frac{2\sigma}{r_{cyl}}\left(T^4 - T_{amb}^4\right) - \frac{2h_c}{r_{cyl}}(T - T_{amb}) \tag{7}$$

where C_V is the Einstein approximation of the total heat capacity of the mixture of nanoparticles, in units of $\mathrm{J{\cdot}m^{-3}{\cdot}K^{-1}}$. In this high temperature approximation, C_V depends only on the number of atoms and is, therefore, independent of the temperature and composition. The first term on the right-hand side accounts for any external heating source (resistive, laser, etc.) in the form of a power density, P, which, in our calculations, is applied uniformly within the first unit-cell only to initiate the system. The second term represents the heat of reaction, with q being the heat of combustion in units of J/released atom-mole of oxygen, pondered by the oxygen flux ϕ that connects macroscale propagation to the elemental particle reaction. The third term gathers all latent enthalpy (H) variations due to various

phase changes such as the melting, evaporation and decomposition of the species, with the specific molar enthalpy h_j of the mechanism j.

$$\mathrm{H} = \sum h_j \, \Gamma\left(T - T_j\right) \tag{8}$$

T_j, is the temperature at which the phase change occurs, and Γ is the step Heaviside function. The fourth term is the energy transferred due to thermal conduction in the material. The way this macroscopic term is formulated is one focus of the present paper, particularly in the way an efficient conductivity term can translate the micro-nanostructure of the thermite material (such as the conductivity term given and discussed in the following Equation (9)). The last two terms are expressing losses in the radiative and convective form where the Stefan–Boltzmann constant is in $\mathrm{W{\cdot}m^{-2}{\cdot}K^{-4}}$ and h_c, the convection coefficient, in $\mathrm{W{\cdot}m^{-2}{\cdot}K^{-1}}$. The factor $2/r_{cyl}$ accounts for the fact that radiative and convective losses occur at the boundaries of the cylindrical system. In Equation (7), we have neglected the radial dependence of the temperature. This is justified by the high conductivity with respect to heat losses. Indeed, the radius of the system is always much smaller than the ratio λ/h_c. No envelope is considered at the system boundaries since our objective is a generic study of different thermite couples independent of the experimental geometry.

2.3. System and Simulation Set-Up

A constant power density, P, of 22 W is applied at the first cell with a system-wide convection coefficient of 100 $\mathrm{W{\cdot}m^{-2}{\cdot}K}$ until initiation. The cell is considered initiated once the runaway exothermic combustion reaction takes precedence over the external heating ramp—this is calculated as surpassing a minimum initiation temperature with a rapid temperature rise. This condition is customized for each fuel/oxidizer pairing as the variable heat capacities affect the initial heating ramp for a given power density, P, as well as the different heat of reactions for each combustive pair. The initiation delay is defined as the time for initiation to occur in the first, externally heated cell. Initially, the entire system is at the ambient temperature (300 K). As the model does not account for reactions in the gas phase, the reaction is stopped when reactants or products are vaporized. A temperature limit, corresponding to the lowest vaporization temperature among the different materials constituting each considered thermite couple, is therefore imposed, after which the system is considered to have dispersed into the environment. These vaporization temperature limits and corresponding materials are listed in Table 1. Other main parameters that have been used for the calculations are listed in the Supplementary Information file S1.

Table 1. Calculated system disruption, defined as the temperature of first vaporization among all thermite basic components, effective thermal conductivity, initiation temperature, initiation delay, and burn rate for Al, B, and Zr fuel based nanothermites.

Fuel Species	Oxide Species	Disruption Temperature in K/(Associated Vaporized Species)	Conductivity ($\mathrm{W{\cdot}m^{-1}{\cdot}K^{-1}}$)	Initiation Temp (K)	Initiation Delay (ms)	Burn Rate ($\mathrm{cm{\cdot}s^{-1}}$)
Al	CuO	2070 (Cu_2O)	2.9	943	91	60
	Fe_2O_3	2743 (Al)	6.7	1994	350	38
	WO_3	1973 (WO_3)	1.6	718	63	17
	Pb_3O_4	1808 (PbO)	1.6	1194	127	2.1
B	CuO	2070 (Cu_2O)	2.4	1285	192	4.3
	Fe_2O_3	2130 (B_2O_3)	5	1577	360	17
	WO_3	1973 (WO_3)	1.4	1228	186	14.5
	Pb_3O_4	1808 (PbO)	1.3	1192	165	8
Zr	CuO	2070 (Cu_2O)	2.6	1643	270	6.7
	Fe_2O_3	3135 (Fe)	6.8	1957	334	37
	WO_3	1973 (WO_3)	1.5	1862	245	14.3
	Pb_3O_4	1808 (PbO)	1.5	no initiation	no initiation	no initiation

This work includes a number of metallic fuel and metal oxides that are utilized to form the thermite materials, namely Al, B, and Zr for the metal fuels and CuO, WO_3, Fe_2O_3, and Pb_3O_4 for the oxide materials. Their main chemical reactions are detailed in the Supplementary Information file S2. These different thermite couples are benchmark tested using identical parameters for comparison. We only consider stoichiometric mixtures of thermites composed of nanoscale fuel and oxidizer particles. All fuel particles are considered 80 nm in diameter with oxidizer sizes spanning from 90 to 120 nm calculated according to the stoichiometric ratio ($\zeta = 1$) (detailed particle sizes are given in the Supplementary Information Table S2). Thermite mixtures are placed in a 3 mm long open-air system, considered with an axisymmetric geometry (2 mm in diameter). The one-dimensional mesh size is set at $\Delta x = 1$ µm, and populated at a %TMD of 60% compaction to place ourselves in a conductively dominant reaction regime. Previous simulations have shown that the overall Al-O reaction is not the limiting factor in Al oxidation [39,49,54–56], which is also consistent with DFT calculations showing the spontaneous reaction of aluminum when in contact with freed oxygen atoms [57]. Therefore, an arbitrary high speed of the oxidation reaction is chosen at the Al/Al_2O_3 interface, with a 3000 $m{\cdot}s^{-1}$ velocity (see Reference [39] for more details). All reactions are continued until a vaporization temperature is reached, at which we consider that the system is disrupted and disperses into the gas phase environment, or all reactants are used.

Following the general structural scheme given in Figure 1 top figure, the state of reaction within each cell is considered physically and thermally homogeneous; as such, the coupled equations (Equations (1) and (7)) are numerically solved in each individual cell by the finite difference method. Then, the reaction propagation is treated as a conductive term between cells, defined by an effective conduction coefficient in $W{\cdot}m^{-1}{\cdot}K^{-1}$, which will be detailed in the next subsection. A steady state establishes when the velocity stabilizes over cells during propagation, which consequently allows determining the burn rate.

2.4. Effective Conduction Coefficient Calculation

Considering a conductively dominant propagation, the expression of the thermal conductivity as expressed in the heat equation (see λ term in Equation (7)) is of crucial importance; indeed, its detailed formulation can traduce the way matter is organized at a lower granularity (micro/nanostructure). We first consider a perfect one-dimensional chain of contacting, alternating (noted as *ca*) particles of the fuel and oxide species as seen in Figure 2. The associated thermal conductivity, λ in Equation (7), is now replaced by λ_{eff}^{ca}, which is written as:

$$\frac{1}{\lambda_{eff}^{ca}} = \frac{d_{ox}\left(3R_{ox}^2-(IO_{ox})^2\right)+ d_{fuel}\left(3R_{fuel}^2-\left(IO_f\right)^2\right)}{\%TMD\times 6\left(O_{ox}O_f\right)^2} \times \left[\frac{1}{\lambda_{ox}R_{ox}} ln\ \frac{(IA_{ox})}{(R_{ox}-IO_{ox})} + \frac{1}{\lambda_{fuel}R_{fuel}} ln\ \frac{\left(IA_f\right)}{\left(R_f-IO_f\right)}\right] \quad (9)$$

where λ_{ox} and λ_{fuel} are the thermal conductivity of the oxidizer and the fuel, respectively (in $W{\cdot}m^{-1}{\cdot}K^{-1}$). Other geometric parameter are defined as shown in Figure 1.

Figure 2. Schematic of an alternating chain of reactant particles from which an effective conduction coefficient is derived.

Equation (9) is obtained by expressing the heat flux across the two-particle interface as a function of the temperature difference between the centers of the particles. The heat flux is calculated in the same manner as the mass transport flux (see Equations (1) and (2)), replacing concentrations by the temperature and the diffusion coefficient by the thermal conductivity. The same logarithmic behavior is observed. In this configuration, most oxide

species of low conductivity will act as a bottleneck to the overall heat conduction and, thus, the initiation and propagation of the system. Note that the compaction is introduced explicitly in this formulation in the first term of Equation (9). Alternative expressions of the thermal conductivity will be introduced in the discussion section of the paper.

3. Results and Discussion

3.1. Benchmark Study

In the following, for all considered thermite couples, the initiation delay, temperature and burn rate are reported in Table 1, with some highlighted materials properties. We also consider a disruption temperature which is defined as the temperature limit above which the body of thermite material is dispersed away from its original state (position and structure). In other words, considering an open system, disruption causes the thermite to be dispersed into the environment. Therefore, at the disruption temperature, the energetic reaction of the system is stopped. This phenomenon has been introduced in a previous work on thermite nanolaminates [49]. The disruption temperature is assumed to match the lowest vaporization temperature of all materials present in the nanothermite (see Table 1). Overall, the best performances are obtained with aluminum as a fuel. Apart from iron oxide, which shows specific behavior across all fuels, aluminothermites (thermites with Al as fuel) are the only fuel group tested that can exhibit initiation delays below the 100 ms regime. Initiation temperatures are also the lowest, in the 900–1000 K range (with the exception of iron oxide). And finally, aluminothermites have high burn rates, notably for the CuO oxidizer, which obtains the highest burn rate of all tested cases (60 $cm{\cdot}s^{-1}$). Thermite reactions can be primarily governed by the oxygen diffusivity through its oxidized fuel, the reaction product, which may act as a barrier for the reacting species to meet and react. Even though the oxidizer is usually chosen for its relative metastability, its decomposition or simply its ability to provide an easy pathway for migrating oxidizing species towards the fuel and its oxide may temper the role of the oxidized fuel barrier layer as the leading parameter, as we will see for most cases apart from CuO. Obviously, the thermal conductivity as well as the reaction enthalpy are other important parameters. This multiplicity of components makes it very difficult, if not impossible, to quantitatively predict a priori the reaction behavior of a given thermite. We will now discuss each considered thermite into more detail.

Aluminothermites—Al/CuO is probably the most studied nanothermite couple in powder form, we have shown that under usual initiation conditions (10^5 K s^{-1}) condensed phase mechanisms correctly match experimental results in term of initiation [5,39]. For the present Al/CuO simulated experiment, the initiation delay, 91 ms at 943 K, is roughly one order of magnitude higher than in Reference [39], in the millisecond range, using similar nanoparticle sizes. Indeed, in that base model, all heat losses, both towards an adjacent cell for propagation and into the environment, were neglected. In this full propagation version, the model contains an explicit treatment of packing and losses due to conduction, convection, and radiation that slows down the temperature rise upon external heating and, consequently, the chemistry of initiation.

The calculated steady state burn rate is established at 60 cm s^{-1} (see Figure 3a). Calculations agree fairly well with the work by Wang et al., where high-speed microscopy permitted in-operando observation of the propagation reaction on a local and macroscopic scale [36]. The authors distinguish a rapid (50 $cm{\cdot}s^{-1}$) microscopic combustion process due to sintering within the flame front, i.e., a purely condensed phase process, from a much slower propagation regime, 3.3 $cm{\cdot}s^{-1}$, observed macroscopically. Interestingly, a simulation with parameters corresponding to their experimental setup, with a 85 nm fuel diameter, 98 nm oxide diameter, ζ = 1.2, and an imposed conductivity of 0.1 $W{\cdot}m^{-1}{\cdot}K^{-1}$, as determined by the authors, leads to a drop of the reaction propagation speed down to 8.5 $cm{\cdot}s^{-1}$, agreeing fairly well with the balance of micro versus macro burn rates.

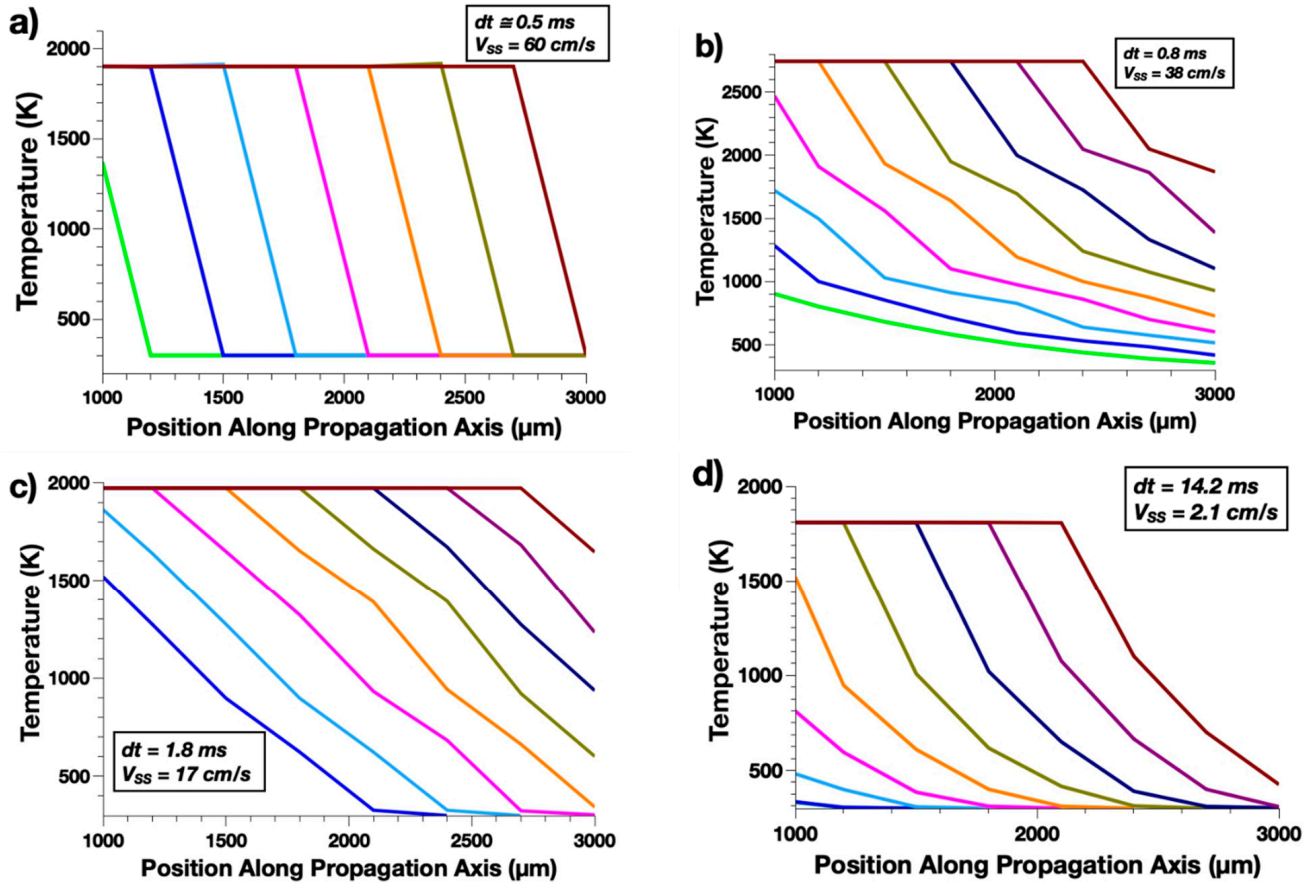

Figure 3. Temperature profiles taken at regular time intervals dt and calculated burn rate V_{SS} for: (**a**) Al/CuO, (**b**) Al/Fe_2O_3, (**c**) Al/WO_3, and (**d**) Al/Pb_3O_4.

Following the kinetics of the various species in a given reacting unit cell of the system (see Supplementary Information file S3), we observed that at the disruption temperature, only 22% of the Al reservoir is consumed. This is consistent with the fact that Al/CuO is known to produce a lot of gases and possibly fragments or aggregates that continue to burn in the atmosphere.

Ferrous oxide (Fe_2O_3) is another oxide material of great technological interest due to its high exothermic performance with reduced gas production in thermite couples (0.14 g of gas per 100 g of thermite mixture) [58]. Extensive studies have characterized the Al/Fe_2O_3 thermite reactions or isolated Fe_2O_3 reduction finding complex decomposition scenarios that were not found to vary with the stoichiometry of the system. One study in particular by Duraes et al., followed by more recent studies, used X-ray diffraction and spectroscopy to analyze the intermediate products present in the reaction [59–62]. While the main products found were alumina and iron, the significant presence of $FeAl_2O_4$ among other intermediate components, led the authors to propose a reduction scheme where Fe_2O_3 reduces first to both Fe_3O_4 and FeO, before a final reduction to pure iron. Therefore, similarly to the Al/CuO thermite, our model assumes a two-step decomposition in which Fe_2O_3 first decomposes into FeO and then further reduces to Fe (see individual reaction equations in the Supplementary Information file S2). Looking at the propagation simulation results plotted in Figure 3b, the Al/Fe_2O_3 system shows a significantly greater initiation delay (350 ms) and temperature (1994 K) compared to Al/CuO. This is not surprising considering that the diffusion of oxygen species within these species have distinct diffusion kinetics; in our model, we assume decomposition kinetics of the oxidizers to follow inner oxygen diffusion characteristics (see Supplementary Information file S1). Consistent with its diffusion properties, iron oxide is known to have a decomposition temperature, 1808 K,

significantly higher than that of CuO (933 K for the bare oxidizer, 1050 K for Al/CuO thermite) [28]. In summary, the ability of iron oxide to release oxygen species dominates the initiation performances, which is radically different from Al/CuO that is driven by oxygen transport through the aluminum oxide barrier layer.

Furthermore, the Al/Fe_2O_3 system has a calculated burn rate in the same range (slightly lower) as the Al/CuO case with a value of 38 cm·s^{-1}, with well-established steady-state propagation (see Figure 3b). Considering the lower enthalpy of reaction (281.7 kJ per oxygen atom) compared to that of Al/CuO (397.5 kJ per oxygen atom), some other effects are probably playing an active role in sustaining a relatively high flame velocity (the second highest value of all tested thermites after Al/CuO). On the one side, Al/Fe_2O_3 combustion can endure a much higher flame temperature due to the high disruption temperature (Al vaporization), which de facto increases all mechanisms kinetics; this effect of the disruption temperature increase leading to a higher burn rate is well-documented in Reference [49] for nanothermites in the form of nanolaminates. On the other side, the thermal conductivity is approximately three times that of Al/CuO, which causes preheating of the non-reacted thermite during the long period of initiation. This process is clearly visible in Figure 3b, as a spatial spreading of the flame front temperature is visible in comparison to that of Al/CuO. For Al/Fe_2O_3, the flame extends over ~800 µm while it is only of 200 µm for Al/CuO (defined as the spatial extension between temperature at its maximum and its upfront thermalization, at a given time of the steady state propagation). To quantify the role of this later process, we artificially reduce the conduction of iron oxide-based thermite to the value of Al/CuO. The calculated burn rate of this Al/Fe_2O_3 thermite with λ_{AlCuO} is 19.7 m·s^{-1}, roughly one-third of the Al/CuO thermite burn-rate, and with minimal change to the initiation delay. Importantly, this indicates that conductivity, rather than the flame temperature, allows a reasonably high burn rate in Al/Fe_2O_3.

The Al/WO_3 couple presents another relatively low-gas production nanothermite with only 0.14 mol of gas produced per 100 g of thermite mixture [58]. The initiation temperature is calculated at 718 K, the lowest value of all of the considered Al-based thermites, just below that of the Al/CuO couple. WO_3 exhibits a higher inner diffusion rate for oxygen atoms to diffuse towards aluminum and its oxide. As a consequence, this thermite falls within the same category as Al/CuO, i.e., thermites in which initiation is governed by the mass transport across the aluminum oxide barrier layer. This allows an initiation delay as low as 63 ms, the lowest of all considered thermites, lower than that of Al/CuO, which is due to the fairly larger amount of elementary exothermic reactions in this delay, as more oxygen is provided by the oxidizer at equivalent temperature. In addition, the slightly lower conductivity (1.6 vs. 2.9 for stoichiometric Al/CuO) is a mean to locally concentrate the energy into hot points in place of the flame front. The burn rate shows a well-established steady state (see Figure 3c) at the value of 17 cm·s^{-1}, lower than that of both Al/Fe_2O_3 and Al/CuO cases, principally because of a poor thermal conductivity. With the enthalpy of reaction being in the range of Al/Fe_2O_3, 277 kJ per oxygen atom, a higher burn rate should be expected, but the much lower disruption temperature, 1973 K, 100 K lower than Cu_2O, is penalizing.

The Al/Pb_3O_4 is an uncommon nanothermite mixture as it contains lead; however, some sectors such as mining continue to use this oxide [46,63]. The heat of reaction is remarkably high, but the vaporization temperature that limits the overall system temperature during combustion is the lowest of all considered aluminothermites, 1808 K, corresponding to the vaporization of PbO. Interestingly, this thermite offers a sort of compromise between the Al/Fe_2O_3 and Al/CuO cases. The enthalpy of reaction and conductivity are more in the range of Al/CuO (see Table 1 and Supplementary Information file S2) while the oxygen supply is limited by the oxidizer, as in Al/ Fe_2O_3. The oxygen diffusivity in the reduced oxide, PbO, is much lower than that of Al_2O_3, in the range of 10^{-9} m^2·s^{-1} (versus 10^{-4} m^2·s^{-1} for alumina) even though it is thermally activated at lower temperature with an activation energy of 93.7 kJ·mol^{-1} (versus 140 kJ·mol^{-1} for alumina, see Supplementary Information file S1). This dual effect, low activation, but limited oxygen flux leads to an

initiation time of 127 ms, higher than that of the Al/CuO thermite, but still much lower than for Al/Fe_2O_3. The limited burn rate value, 2 cm·s^{-1}, is associated with a poor thermal conductivity. Note that in all Al-based thermites tested, the steady state is always achieved. In addition, they all reach their disruption temperature. As Al/Pb_3O_4 possesses the lowest disruption temperature, corresponding to the vaporization of PbO (1808 K), the burning of the remaining thermite materials is operated in the gas phase, which is consistent with the high level of gas production reported for this thermite (0.84 g of gas per g of thermite), almost at the level of Al/I_2O_5, which is one of the best-known thermites for gas generation.

Boron-Based Thermites—Boron thermites have attracted less attention despite high gravimetric as well as volumetric energy densities, nearly equivalent to those of aluminum [58,64]. The amount of gas produced using B is generally slightly lower than that of Al based thermites; the B/Fe_2O_3 couple is actually found to produce negligible gas, making it a high contender for gasless thermite applications [58,64]. Boron is known to be difficult to initiate for combustion, which is expected due to its native oxide shell that exhibits low oxygen diffusivity compared to alumina (see Supplementary Information file S1). In addition, boron thermites also have the overall lowest elemental heat of reaction of all the thermite reactions considered in this study, (104–244 kJ/mol of atomic O depending on the couple) compared with aluminum-based thermites (277–397 kJ/mol of atomic O). The consequence is that the overall performances are decreased by an order of magnitude compared with aluminothermites; initiation delays all exceeded 150 ms (the highest value being 360 ms for B/Fe_2O_3), and burn rates decreased down to the cm·s^{-1} range. This may be the main reason for primarily restricting the use of boron to use as an additive, motivated by its volumetric energy density [65].

B/CuO offers one of the weakest performances (lowest burn rate of all boron-based thermites). The calculated initiation time is 192 ms, which is more than twice that of Al/CuO, with a consistently higher initiation temperature (1285 K for B/CuO). This value corresponds well to experimental values found by Huang et al. with initiation delays of 125 ms for a stoichiometric mixture of particles being 500 nm and 50 nm in diameter for boron and CuO, respectively, as a compressed pellet in a constant-volume vessel [64]. The calculated burn rate is also low: 4.3 cm·s^{-1}. Both the low initiation time and burn rate values are caused by the low level of oxygen flux supplied to the fuel, as the thermal conductivity value is not very different from that of Al/CuO. The low reaction enthalpy is also contributing to the weak performance.

With iron oxide, the initiation time is multiplied by a factor of two compared to B/CuO, with an ensuing rise in the initiation temperature to 1577 K. The value of 360 ms, which qualitatively corresponds well with the increase seen experimentally, makes it the slowest in reactivity of all tested thermite couples [64]. Once self-sustained reaction is reached, this couple has the highest flame velocity for this fuel at 17 cm.s^{-1}, which corroborates the fact that thermal conductivity is a crucial factor in the burn rate property, allowing the preheating of the upfront reaction zone.

With nearly equivalent thermal conductivity, tungsten and lead oxides show similar initiation delays (186 and 165 ms, respectively), slightly lower than that of B/CuO (~192 ms), with comparable initiation temperatures (~1200K). The burn rate of B/WO_3, 14.5 cm.s^{-1}, is almost twice that of B/Pb_3O_4, 8 cm.s^{-1}, despite B/Pb_3O_4 having the highest enthalpy of reaction of all tested cases with Boron as a fuel. This is due to the extremely low diffusivity of oxygen within the reduced PbO oxide, which likely becomes the limiting step of the reaction. Similar to aluminothermites, all boron-based couples show a clear steady state propagation, reaching their disruption temperature (see Figure 4), once the steady state regime is established.

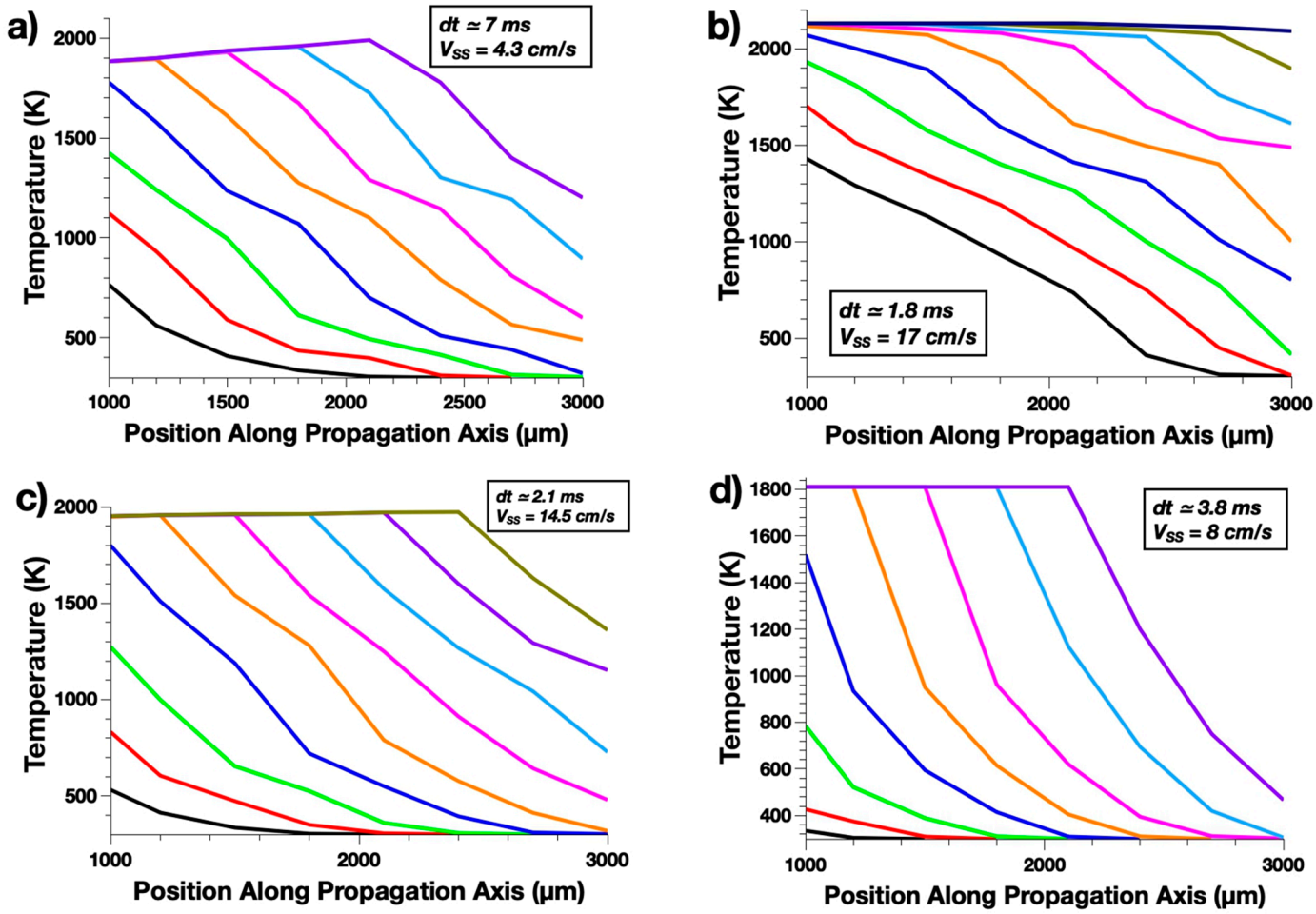

Figure 4. Temperature profiles taken at regular time intervals dt and calculated burn rate V_{SS} for: (**a**) B/CuO, (**b**) B/Fe_2O_3, (**c**) B/WO_3, and (**d**) B/Pb_3O_4 systems at ξ = 1.0 with 80-nm boron particles.

Zirconium-Based Thermites—In a similar capacity to boron metal, nanosized zirconium has been proposed as an additive to improve the properties of conventional Al micron-sized fuel, with these three-material composite thermites showing higher reactivity in terms of initiation time, increased energy delivery and longer combustion duration [66]. Importantly, the poor oxygen diffusivity across ZrO_2, the lowest of all considered fuels in the initiation temperature range (1000–2000 K, see Supplementary Information file S1) is a strong limit to the reactivity of thermites using only Zr as the fuel, even more limiting than the case of boron, which also exhibits difficulties for initiation for the same reason. This leads to longer initiation times and temperatures despite similar thermal conductivities compared with aluminum and boron-based thermites in most cases. Initiation times exceed 200 ms for all systems. Note that Zr/Pb_3O_4 cannot be initiated under these conditions, requiring an initiation/propagation formulation that relies solely on gas phase mechanisms for systems brought to the disruption temperature. At this time, there are no explicit studies on the reaction characteristics of purely zirconium-based systems, and so the results will be discussed in comparison with the other fuel propositions.

It is interesting to note that the CuO oxidizer gives again the slowest propagating reaction when mixed with Zr fuel: 6.7 cm·s^{-1} as in the case of B fuel. It is probable that the relatively low vaporization limit for this system at 2070 K (Cu_2O) is not sufficiently hot to allow enough freed oxygen to escape into the fuel particle until just before the system disruption. CuO is generally a high gas-producing oxidizer, and, thus, this couple would likely see enhanced performance in experimental studies or in multiphasic simulations including gas phase reactions. The Zr/Fe_2O_3 thermite couple shows comparable behavior

to the other thermite couples utilizing this oxide (see Figure 5). The reaction remains dominantly driven by the decomposition of Fe_2O_3 at the high temperature of 1957 K. This is similar to Zr/CuO that does not see high flux of oxygen towards the Zr fuel, necessary for the runaway reaction to initiate until this high temperature. However, this system is limited by a much higher vaporization temperature at 3135 K for the final Fe product, which allows more time for the oxidation of the fuel, and more activation for diffusion, before the disruption temperature is reached. This couple was found to have the highest propagation rate at 37 $cm \cdot s^{-1}$. It is interesting to note that this propagation velocity is as fast as that of the Al/Fe_2O_3 thermite, despite the large difference in oxygen diffusivity between Al_2O_3 and ZrO_2, and the very similar heats of reactions (275 vs. 281 $kJ \cdot mol^{-1}$ for Zr/Fe_2O_3 and Al/Fe_2O_3, respectively). In contrast to the limitation of the Zr/CuO system, the very high oxygen diffusivity in WO_3 at low temperature likely moderates the deficit caused by limited diffusion through the native oxide layer. The freed oxygen reservoir is available in this case to maximize the oxidation of the fuel from about 800 K. This is still significantly smaller than the comparative temperature gradients of this oxide coupled with the other fuels.

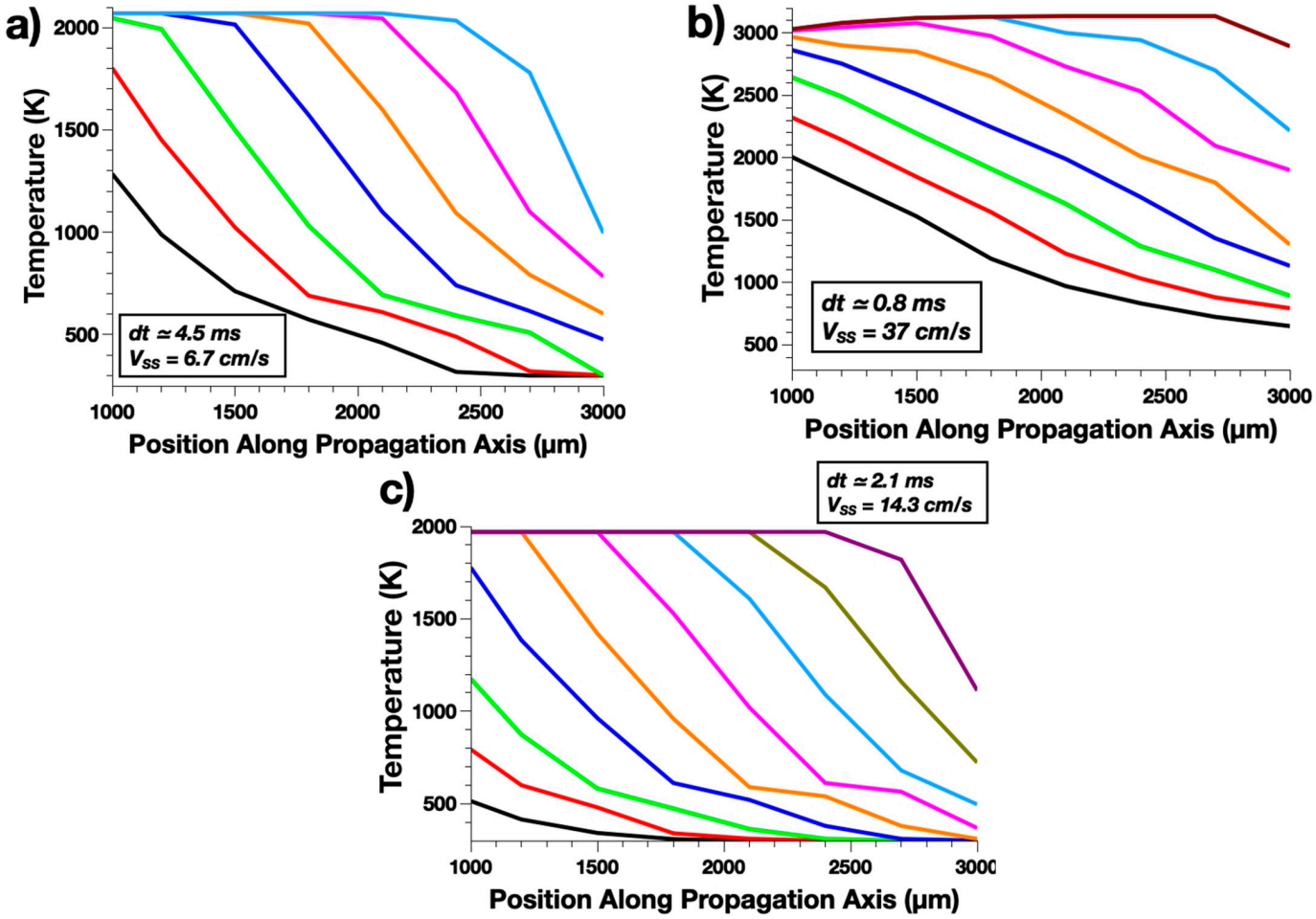

Figure 5. Temperature profiles taken at regular time intervals dt and calculated burn rate V_{SS} for (**a**)Zr/CuO, (**b**) Zr/Fe_2O_3, and (**c**) Zr/WO_3, systems at ξ = 1.0 with 80-nm Zr particles.

Finally, the Zr/Pb_3O_4 couple was the only thermite considered that does not manage to initiate under the simulated conditions. This is ultimately unsurprising given the extremely low oxygen diffusivity in both species acting as a complete bottleneck to the initiation of the self-sustaining reaction. Combined with the very low vaporization temperature of PbO

(1808 K), the diffusivity of oxygen in ZrO_2 and Pb_3O_4 only reach a maximum of 1.7×10^{-13} and 9.88×10^{-12} $m^2 \cdot s^{-1}$, respectively, before the disruption of the nanostructured system.

Overall, the results highlight the role of oxygen mass transport and thermal conductivity on the initiation time and burn rate. It is observed that mass transport has a major impact on both properties, while conductivity more specifically is beneficial to the burn rate. However, the simulated losses are largely underestimated compared with most real experiments. We do not consider effects of the substrate or envelope, which are known to play an essential role.

In the following, we discuss the effect of heat transport in more details, by modifying the effective conductivity.

3.2. Effective Thermal Conductivity Formulation

The preceding results are based on a model system in which the thermal conductivity is expressed (see Equation (4)) as a function of the compaction (%TMD) in the case of a perfect alternation of metal/metal oxide nanoparticles organized as a linear chain of homogeneous nanosized spheres (see Figure 2). From the literature, another common way to treat thermal conductivity of thermites is to consider an averaged and homogeneous bulk associating both the fuel and oxidizers (see Figure 6). Focke et al. suggested such an effective thermal conduction expression, considering a continual heat flow through the compressed powder, which corresponds to a bulk material with the combined thermal properties of the fuel and the oxide species (o, oxidizer; f, fuel), given by [46]:

$$\lambda_{eff}^{b} = \varepsilon_o \lambda_o + (1 - \varepsilon_o)\lambda_f \tag{10}$$

with ε_o and $(1 - \varepsilon_o)$ being the mass fraction of the oxide and fuel species, respectively, in a fully dense system. To modify this value to account for an actual experimental %TMD compaction, we have slightly adjusted the formula to:

$$\lambda_{eff}^{b} = \varepsilon_o \lambda_o + (\%TMD - \varepsilon_o)\lambda_f \tag{11}$$

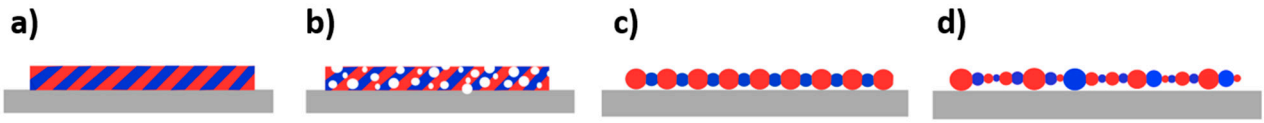

Figure 6. One-dimensional diagrams of the "effective" material structure given by: (**a**) bulk material with combined thermal properties, (**b**) bulk material with voids filling space to %TMD, (**c**) single 1D chain of identical alternating fuel and oxide particles, and (**d**) a single one-dimensional chain of various sized alternating fuel and oxide particles.

In this case, the material is still treated as a bulk heterogeneous material, but now the energetic mixture is having voids up to the preset %TMD (Figure 6b). Both of these approaches do not consider the geometric factors that form the basis of this model, the sintered particle pair, in addition to be best fit for simulating a %TMD that is rarely seen in nanothermites (>60%). Note also, that these effective conductivities ignore the interfacial regions formed by the wetted contact between the fuel-oxide pairing, whose bottlenecking aspect is important at the scale of the diffusion/reaction equations in our model. A more elaborate version of Equation (9) considers the realistic diversity of non-constant particle sizes, as seen in the size distribution of an actual nanopowder, as well as the assortment of different sized agglomerates formed after reactive sintering. This formulation as shown in Figure 6d is:

$$\frac{1}{\lambda_{eff}^{d}} = \frac{1}{6\%TMD} \sum_i \left(\frac{1}{R_i \lambda_i} ln \left[\frac{R_i + (IO)_i^+}{R_i - (IO)_i^+} \times \frac{R_i + (IO)_i^-}{R_i - (IO)_i^-} \right] \times \frac{\sum \left[d_i^+ \left(3R_i^2 - (IO)_i^{+2} \right) + d_i^- \left(3R_i^2 - (IO)_i^{-2} \right) \right]}{L^2} \right) \tag{12}$$

In this formulation, each particle possesses two moving interfaces from both sides of the chain axis. R_i is the radius of the particle i (i being the oxidizer or fuel). d_i^+ and d_i^- are the converted materials being oxidized or reduced depending on the chemical nature of particle i, + and – indicating the two opposite directions along the linear chain axis, from either sides of the center of particle i, as defined in the Supplementary Information file S4. L is the length of the considered chain motif. Equation (7) is the generalization of Equation (4) to systems with different nanoparticle sizes. Here, the heat flux is expressed as a function of the temperature difference along a chain of sintered nanoparticles. For this reason, Equation (7) contains a sum representing all discrete interfaces between nanoparticles, which can be modified depending on the actual structure considered. Note that when this effective conductivity is used, the particle size distribution is exclusively accounted for in the conduction, while the particle sizes considered for all mass transfer mechanisms remain constant.

Table 2 compares the effect of the four above expressions of the conductivity. It assembles calculated initiation and combustion performances in terms of the initiation temperature, initiation delay, and burn rate relative to the proposed effective thermal conduction coefficient. We make use of a typical model set up of 80 nm Al: 99 nm CuO system (ξ = 1.0) at 60 %TMD unless otherwise mentioned. A bulk-like term (Equation (5)) accounting for a fully dense, 100%TMD packing, shows the highest conduction coefficient (83 W/mK) leading to a high burn rate value, at 22 $m{\cdot}s^{-1}$. The high conductivity is a slightly penalizing initiation because of the energy loss from the externally heated first cell into the broader apparatus (higher initiation delay, 85 ms). This also results in a slightly higher initiation temperature (1003 K). Next, using the formulation given in Equation (6), which introduces compaction, all values are reduced. The burn rate is divided by two, because the conductivity drops down to 50 $W{\cdot}mK^{-1}$. This lower conductivity limits losses into the system that leads to a slightly lower initiation temperature, lowering the initiation delay down to 69 ms. In contrast to bulk like formulations, shifting to chain like structured materials, more in the scope of the considered nanostructure (Equations (4) and (7)), reduces the conductivity by an order of magnitude. The conductivity through the interfaces between oxide particles that traditionally have a smaller bulk thermal conductivity can bottleneck the heat propagation, slowing the overall burn rate issued from the self-sustained reaction. This modification greatly affects performances in comparison to homogeneous and dense materials. The burn rates drop into the $cm{\cdot}s^{-1}$ range. We saw previously that the homogeneous alternated chain has a 59 ms initiation and that both of these values fall within recently published data [36]. Equation (7) accounts for a distribution of different sized particles in the chain, which gives a more realistic picture of the experimental system in actual fabricated powders, offering an opportunity to quantify its impact on performances. Additionally, the numerous studies of in situ observation of reactive sintering has shown that the formation of microscale components due to agglomeration of nanoscale individuals occur on a faster timescale than that of the overall reaction, meaning some nanoscale material coalesces before initiation [36].

Table 2. Calculated initiation and combustion performances for a thermite system of 80 nm Al: 99 nm CuO (ξ = 1.0) at 60 %TMD (except for * which is 100 %TMD) considering the different effective conductivity formulas.

Formulation/Figure 6 Scheme	Effective Conduction Coefficient ($W{\cdot}mK^{-1}$)	Initiation Temperature (K)	Initiation Delay (ms)	Burn Rate ($cm{\cdot}s^{-1}$)
Equation (5)*/a)	83.3	1003	85	22
Equation (6)/b)	50.2	997	69	11
Equation (4)/c)	2.9	944	59	0.6
Equation (7)/d)	0.6–1.2	943	23–42	0.2–0.3

Multiple size dispersions of either just the fuel particles, just the oxide particles, or both were tested (see Supplementary Information file, Table S5). The dispersion was set up as a half-Gaussian distribution with the mean set to the average particle size utilized in these studies (i.e., 80 nm for aluminum and 100 nm for cupric oxide). Each effective conductivity reported in Table S5, corresponding to a certain variance, was defined as the average of three calculations with a different seed value utilized to generate the random diameter samples. This led to a variety of effective conductivities that were simulated to find their corresponding reaction characteristics. A summary of these system features is provided in the Supplementary Information file S5. With regards to the speed of propagation for these varied systems, all fall within an acceptable order of magnitude relevant to the recent studies on the nanothermite reaction from Wang et al. [36] (see Table S3 and Table 2). From the lowest conductivity (0.599 for a variance of 250 on the only Al-particles) to the highest (1.2 for a variance of 300 on both fuel and oxide particles), the difference in the propagation velocity does not exceed 50%. Additionally, the difference between the burn rate for the system where both particle sizes are randomly distributed and for the system with fixed particles sizes, is only reaching 0.30 $m{\cdot}s^{-1}$. The effective conductivity calculated with these distributions was 1.21, the highest of the size dispersed systems considered in this paper. It is interesting to note that, contrary to the isolated distributions for Al or CuO, the larger particle size distribution leads to a relatively high conductivity. This is a direct consequence of considering the geometric factors, and importantly sintering in the formulation, as two larger particles in contact will share a larger interfacial region through which heat can propagate at a faster speed. However, overall results do not show deep changes in what concerns initiation temperature and delay or the burn rate. Therefore, it can be concluded that the size dispersion does not severely influence the initiation nor the propagation behavior.

4. Conclusions

This paper reports on the modelling of the initiation characteristics and the burn rate of a series of thermites combining Al, B, and Zr fuels with CuO, Fe_2O_3, WO_3, and Pb_3O_4 oxidizers. The model assumes a combustion process that is exclusively based on condensed phase processes, including the diffusion and reaction of species. Stoichiometric mixtures with 60% compaction are systematically compared and discussed in light of their thermal conductivity, ability to transport oxygen species, reaction enthalpies, and the more complex disruption temperature, which assumes that the combustion is stopped at the destruction of the initial thermite structure, causing the combustion to continue in the gas phase through molecules or thermite fragments, away from their original position. In the present paper, we assumed a disruption temperature equal to the lowest vaporization temperature of the species present in the thermite system. We observed that aluminothermites are the most performant thermites in terms of initiation delay and burn rate, with Al/CuO being the most efficient, having a 90 ms delay in initiation and a 60 $cm.s^{-1}$ burn rate. While both diffusion properties and thermal conductivity are driving initiation, the burn rate is mostly influenced by thermal conductivity, making iron oxide a leading material in boron or zirconium based thermites, despite its high thermal activation to release oxygen. We also develop several formulations for the effective thermal conductivity, to allow for a more realistic description of the way matter is nano-structured. In this scope, the dispersion in size of the nanoparticles is shown to only marginally alter initiation or propagation performances.

Supplementary Materials: The following are available online at https://www.mdpi.com/article/10.3390/app11146553/s1, Supplementary materials associated with this article are available in a separate document.

Author Contributions: Conceptualization, C.R., M.D.R. and A.E.; methodology, S.B., M.D.R.; software, S.B.; validation, S.B., S.C.; writing—original draft preparation, S.B., A.E.; writing—review and editing, S.B., A.E., S.C., M.D.R., C.R.; supervision, A.E., C.R.; funding acquisition, C.R. All authors have read and agreed to the published version of the manuscript.

Funding: C.R. received funding from the European Research Council (ERC) under the European Union's Horizon 2020 research and innovation program (grand agreement No. 832889-PyroSafe).

Acknowledgments: The authors acknowledge support from the European Research Council (H2020 Excellent Science) Researcher Award (grant 832889-PyroSafe) and the Occitanie Region/European Union for their FEDER support (THERMIE grant).

Conflicts of Interest: The authors declare no competing financial interests.

References

1. Koch, E.C.; Knapp, S. Thermites-versatile materials. *Propell. Explos. Pyrot.* **2019**, *44*, 7. [CrossRef]
2. Aumann, C.E.; Skofronick, G.L.; Martin, J.A. Oxidation behavior of aluminum nanopowders. *J. Vac. Sci. Technol. B Microelectron. Nanometer Struct. Process. Meas. Phenom.* **1994**, *13*, 1178–1183. [CrossRef]
3. Rossi, C. Engineering of Al/CuO reactive multilayer thin films for tunable initiation and actuation. *Propellants Explos. Pyrotech.* **2019**, *44*, 94–108. [CrossRef]
4. Dreizin, E.L. Metal-based reactive nanomaterials. *Prog. Energy Combust. Sci.* **2009**, *35*, 141–167. [CrossRef]
5. Sullivan, K.T.; Chiou, W.-A.; Fiore, R.; Zachariah, M.R. In situ microscopy of rapidly heated nano-Al and nano-Al/WO3 thermites. *Appl. Phys. Lett.* **2010**, *97*, 133104. [CrossRef]
6. Wainwright, E.R.; Sullivan, K.T.; Grapes, M.D. Designer direct ink write 3D-printed thermites with tunable energy release rates. *Adv. Eng. Mater.* **2020**, *22*, 1901196. [CrossRef]
7. Pantoya, M.L.; Granier, J.J. Combustion behavior of highly energetic thermites: Nano versus micron composites. *Propellants Explos. Pyrotech. Int. J. Deal. Sci. Technol. Asp. Energetic Mater.* **2005**, *30*, 53–62. [CrossRef]
8. Glavier, L.; Taton, G.; Ducere, J.M.; Baijot, V.; Pinon, S.; Calais, T.; Esteve, A.; Rouhani, M.D.; Rossi, C. Nanoenergetics as pressure generator for nontoxic impact primers: Comparison of Al/Bi_2O_3, Al/CuO, Al/MoO_3 nanothermites and Al/PTFE. *Combust. Flame* **2015**, *162*, 1813–1820. [CrossRef]
9. Wang, L.; Luss, D.; Martirosyan, K.S. The behavior of nanothermite reaction based on Bi_2O_3/Al. *J. Appl. Phys.* **2011**, *110*, 74311. [CrossRef]
10. Piekiel, N.W.; Zhou, L.; Sullivan, K.T.; Chowdhury, S.; Egan, G.C.; Zachariah, M.R. Initiation and reaction in Al/Bi2O3Nanothermites: Evidence for the predominance of condensed phase chemistry. *Combust. Sci. Technol.* **2014**, *186*, 1209–1224. [CrossRef]
11. Rodríguez, G.A.A.; Suhard, S.; Rossi, C.; Estève, D.; Fau, P.; Sabo-Etienne, S.; Mingotaud, A.F.; Mauzac, M.; Chaudret, B. A microactuator based on the decomposition of an energetic material for disposable lab-on-chip applications: Fabrication and test. *J. Micromechanics Microeng.* **2008**, *19*, 015006. [CrossRef]
12. Nicollet, A.; Salvagnac, L.; Baijot, V.; Estève, A.; Rossi, C. Fast circuit breaker based on integration of Al/CuO nanothermites. *Sens. Actuators A Phys.* **2018**, *273*, 249–255. [CrossRef]
13. Piercey, D.G.; Klapooke, T.M. Nanoscale aluminum-metal oxide (thermite) reactions for application in energetic materials. *Cent. Eur. J. Energ. Mat.* **2010**, *7*, 115–129.
14. Staley, C.S.; Raymond, K.E.; Thiruvengadathan, R.; Apperson, S.J.; Gangopadhyay, K.; Swaszek, S.M.; Taylor, R.J.; Gangopadhyay, S. Fast-impulse nanothermite solid-propellant miniaturized thrusters. *J. Propul. Power.* **2015**, *31*, 483. [CrossRef]
15. Chaalane, A.; Rossi, C.; Esteve, D. The formulation and testing of new solid propellant mixture (DB plus x%BP) for a new MEMS-based microthruster. *Sensor Actuat. A Phys.* **2007**, *138*, 161–166. [CrossRef]
16. Puchades, I.; Hobosyan, M.; Fuller, L.F.; Liu, F.; Thakur, S.; Martirosyan, K.S.; Lyshevski, S.E. MEMS microthrusters with nanoenergetic solid propellants. In Proceedings of the 14th IEEE International Conference on Nanotechnology, Toronto, ON, Canada, 18–21 August 2014.
17. Bezmelnitsyn, A.; Thiruvengadathan, R.; Barizuddin, S.; Tappmeyer, D.; Apperson, S.; Gangopadhyay, K.; Gangopadhyay, S.; Redner, P.; Donadio, M.; Kapoor, D.; et al. Modified Nanoenergetic Composites with Tunable Combustion Characteristics for Propellant Applications. *Propellants Explos. Pyrotech.* **2010**, *35*, 384–394. [CrossRef]
18. Swiston, A.J.; Besnoin, E.; Duckham, A.; Knio, O.M.; Weihs, T.P.; Hufnagel, T.C. Thermal and microstructural ef-fects of welding metallic glasses by self-propagating reactions in multilayer foils. *Acta Mater* **2005**, *53*, 3713–3719. [CrossRef]
19. Duckham, A.; Spey, S.J.; Wang, J.; Reiss, M.; Weihs, T.P.; Besnoin, E.; Knio, O.M. Reactive nanostructured foil used as a heat source for joining titanium. *J. Appl. Phys.* **2004**, *96*, 2336–2342. [CrossRef]
20. Zhu, P.; Shen, R.Q.; Ye, Y.H.; Zhou, X.; Hu, Y.; Wu, L.Z. Energetic Igniters Based on Al/CuO/B/Ti Reactive Multilayer Films. Theory and Practice of Energetic Materials (Vol Ix). In Proceedings of the 2011 International Autumn Seminar on Propellants, Explosives and Pyrotechnics, Nanjing, China, 20–23 September 2011.
21. Nicollet, A.; Lahiner, G.; Belisario, A.; Assié-Souleille, S.; Djafari-Rouhani, M.; Estève, A.; Rossi, C. Investigation of Al/CuO multilayered thermite ignition. *J. Appl. Phys.* **2017**, *121*, 034503. [CrossRef]

22. Glavier, L.; Nicollet, A.; Jouot, F.; Martin, B.; Barberon, J.; Renaud, L.; Rossi, C. Nanothermite/RDX-Based Miniature Device for Impact Ignition of High Explosives. *Propell. Explos. Pyrot.* **2017**, *42*, 307–316. [CrossRef]
23. Zhu, P.; Shen, R.; Ye, Y.; Fu, S.; Li, D. Characterization of Al/CuO nanoenergetic multilayer films integrated with semiconductor bridge for initiator applications. *J. Appl. Phys.* **2013**, *113*, 184505. [CrossRef]
24. Sun, J.; Pantoya, M.L.; Simon, S.L. Dependence of size and size distribution on reactivity of aluminum nanoparticles in reactions with oxygen and MoO_3. *Thermochim. Acta* **2006**, *444*, 117–127. [CrossRef]
25. Sanders, V.E.; Asay, B.W.; Foley, T.J.; Tappan, B.C.; Pacheco, A.N.; Son, S.F. Reaction propagation of four nanoscale energetic composites (Al/MoO_3, Al/WO_3, Al/CuO, and Bi_2O_3). *J. Propul. Power* **2007**, *23*, 707–714. [CrossRef]
26. Rossi, C. Two decades of research on nano-energetic materials. *Propellants Explos. Pyrotech.* **2014**, *39*, 323–327. [CrossRef]
27. Zhou, X.; Torabi, M.; Lu, J.; Shen, R.; Zhang, K. Nanostructured energetic composites: Synthesis, ignition/combustion modeling, and applications. *ACS Appl. Mater. Interfaces* **2014**, *6*, 3058–3074. [CrossRef] [PubMed]
28. Hübner, J.; Klaumünzer, M.; Comet, M.; Martin, C.; Vidal, L.; Schäfer, M.; Kryschi, C.; Spitzer, D. Insights into combustion mechanisms of variable aluminum-based iron oxide/-hydroxide nanothermites. *Combust. Flame* **2017**, *184*, 186–194. [CrossRef]
29. Sullivan, K.T.; Kuntz, J.; Gash, A.E. The role of fuel particle size on flame propagation velocity in thermites with a nanoscale oxidizer. *Propellants, Explos. Pyrotech.* **2014**, *39*, 407–415. [CrossRef]
30. Zohari, N.; Keshavarz, M.H.; Seyedsadjadi, S.A. The advantages and shortcomings of using nano-sized energetic materials. *Cent. Eur. J. Energ. Mat.* **2013**, *10*, 135–147.
31. Zapata, J.; Nicollet, A.; Julien, B.; Lahiner, G.; Esteve, A.; Rossi, C. Self-propagating combustion of sputter-deposited Al/CuO nanolaminates. *Combust. Flame* **2019**, *205*, 389–396. [CrossRef]
32. Wu, T.; Lahiner, G.; Tenailleau, C.; Reig, B.; Hungria, T.; Esteve, A.; Rossi, C. Unexpected enhanced reactivity of aluminized nanothermites by accelerated aging. *Chem. Eng. J.* **2021**, *418*, 129432. [CrossRef]
33. Julien, B.; Wang, H.; Tichtchenko, E.; Pelloquin, S.; Estève, A.; Zachariah, M.R.; Rossi, C. Elucidating the dominant mechanisms in burn rate increase of thermite nanolaminates incorporating nanoparticle inclusions. *Nanotechnology* **2021**, *21*, 215401. [CrossRef] [PubMed]
34. Wang, H.Y.; Julien, B.; Kline, D.J.; Alibay, Z.; Rehwoldt, M.C.; Rossi, C.; Zachariah, M.R. probing the reaction zone of nanolaminates at similar to mu s time and similar to mu m spatial resolution. *J. Phys. Chem. C* **2020**, *124*, 13679–13687. [CrossRef]
35. Mursalat, M.; Huang, C.; Julien, B.; Schoenitz, M.; Esteve, A.; Rossi, C.; Dreizin, E.L. Low-temperature exothermic reactions in Al/CuO nanothermites producing copper nanodots and accelerating combustion. *ACS Appl. Nano Mater.* **2021**, *4*, 3811–3820. [CrossRef]
36. Wang, H.; Kline, D.J.; Zachariah, M.R. In-operando high-speed microscopy and thermometry of reaction propagation and sintering in a nanocomposite. *Nat. Commun.* **2019**, *10*, 3032. [CrossRef]
37. Chakraborty, P.; Zachariah, M.R. Do nanoenergetic particles remain nano-sized during combustion? *Combust. Flame* **2014**, *161*, 1408–1416. [CrossRef]
38. Monk, I.; Schoenitz, M.; Dreizin, E.L. The effect of heating rate on combustion of fully dense nanocomposite thermite particles. *Combust. Sci. Technol.* **2017**, *190*, 1–19. [CrossRef]
39. Brotman, S.; Rouhani, M.D.; Rossi, C.; Esteve, A. A condensed phase model of the initial Al/CuO reaction stage to interpret experimental findings. *J. Appl. Phys.* **2019**, 125. [CrossRef]
40. Zhu, Z.-Y.; Ma, B.; Tang, C.-M.; Cheng, X.-L. Molecular dynamic simulation of thermite reaction of Al nanosphere/Fe_2O_3 nanotube. *Phys. Lett. A* **2016**, *380*, 194–199. [CrossRef]
41. Zhang, Y.-Y.; Wang, M.-J.; Chang, C.-R.; Xu, K.; Ma, H.-X.; Zhao, F.-Q. A DFT study on the enthalpies of thermite reactions and enthalpies of formation of metal composite oxide. *Chem. Phys.* **2018**, *507*, 19–27. [CrossRef]
42. Xiong, G.; Yang, C.; Feng, S.; Zhu, W. Ab initio molecular dynamics studies on the transport mechanisms of oxygen atoms in the adiabatic reaction of Al/CuO nanothermite. *Chem. Phys. Lett.* **2020**, *745*, 137278. [CrossRef]
43. Lanthony, C.; Ducere, J.M.; Esteve, A.; Rossi, C.; Djafari-Rouhani, M. Formation of Al/CuO bilayer films: Basic mechanisms through density functional theory calculations. *Thin Solid Film.* **2012**, *520*, 4768–4771. [CrossRef]
44. Lanthony, C.; Guiltat, M.; Ducere, J.M.; Verdier, A.; Hemeryck, A.; Djafari-Rouhani, M.; Rossi, C.; Chabal, Y.J.; Esteve, A. Elementary surface chemistry during CuO/Al nanolaminate-thermite synthesis: Copper and oxygen deposition on aluminum (111) surfaces. *ACS Appl. Mater. Inter.* **2014**, *6*, 15086–15097. [CrossRef]
45. Jacob, R.J.; Hill, K.J.; Yang, Y.; Pantoya, M.L.; Zachariah, M.R. Pre-stressing aluminum nanoparticles as a strategy to enhance reactivity of nanothermite composites. *Combust. Flame* **2019**, *205*, 33–40. [CrossRef]
46. Montgomery, Y.C.; Focke, W.W.; Kelly, C. Measurement and modelling of pyrotechnic time delay burning rates: Method and model development. *Propellants Explos. Pyrotech.* **2017**, *42*, 1161–1167. [CrossRef]
47. Tichtchenko, E.; Estève, A.; Rossi, C. Modeling the self-propagation reaction in heterogeneous and dense media: Application to Al/CuO thermite. *Combust. Flame* **2021**, *228*, 173–183. [CrossRef]
48. Epps, J.M.; Hickey, J.-P.; Wen, J.Z. Modelling reaction propagation for Al/CuO nanothermite pellet combustion. *Combust. Flame* **2021**, *229*, 111374. [CrossRef]
49. Lahiner, G.; Nicollet, A.; Zapata, J.; Marin, L.; Richard, N.; Rouhani, M.D.; Rossi, C.; Esteve, A. A diffusion-reaction scheme for modeling ignition and self-propagating reactions in Al/CuO multilayered thin films. *J. Appl. Phys.* **2017**, *122*, 155105. [CrossRef]

50. Baijot, V.; Mehdi, D.R.; Rossi, C.; Esteve, A. A multi-phase micro-kinetic model for simulating aluminum based thermite reactions. *Combust. Flame* **2017**, *180*, 10–19. [CrossRef]
51. Deal, B.E.; Grove, A.S. General relationship for the thermal oxidation of silicon. *J. Appl. Phys.* **1965**, *36*, 3770–3778. [CrossRef]
52. Sullivan, K.; Piekiel, N.; Wu, C.; Chowdhury, S.; Kelly, S.; Hufnagel, T.; Fezzaa, K.; Zachariah, M. Reactive sintering: An important component in the combustion of nanocomposite thermites. *Combust. Flame* **2012**, *159*, 2–15. [CrossRef]
53. Baijot, V.; Glavier, L.; Ducere, J.M.; Rouhani, M.D.; Rossi, C.; Esteve, A. Modeling the pressure generation in aluminum-based thermites. *Propell. Explos. Pyrot.* **2015**, *40*, 402–412. [CrossRef]
54. Jian, G.; Chowdhury, S.; Sullivan, K.; Zachariah, M.R. Nanothermite reactions: Is gas phase oxygen generation from the oxygen carrier an essential prerequisite to ignition? *Combust. Flame* **2013**, *160*, 432–437. [CrossRef]
55. Zhou, L.; Piekiel, N.; Chowdhury, S.; Zachariah, M.R. Time-resolved mass spectrometry of the exothermic reaction between nanoaluminum and metal oxides: The role of oxygen release. *J. Phys. Chem. C* **2010**, *114*, 14269–14275. [CrossRef]
56. Gao, Y.; Mathilde, I.; Mattson, E.; Lucero, A.T.; Kim, J.; Djafari Rouhani, M.; Chabal, Y.; Rossi, C.; Esteve, A. Al interaction with ZnO surfaces. *J. Phys. Chem. C* **2018**, *122*, 17856. [CrossRef]
57. Lanthony, C.; Ducere, J.M.; Rouhani, M.D.; Hemeryck, A.; Esteve, A.; Rossi, C. On the early stage of aluminum oxidation: An extraction mechanism via oxygen cooperation. *J. Chem. Phys.* **2012**, *137*, 094707. [CrossRef]
58. Fischer, S.; Grubelich, M. *Theoretical Energy Release of Thermites, Intermetallics, and Combustible Metals*; Office of Scientific and Technical Information (OSTI): Oak Ridge, TN, USA, 1998; pp. 231–286.
59. Duraes, L.; Costa, B.F.O.; Santos, R.; Correia, A.; Campos, J.; Portugal, A. Fe2O3/aluminum thermite reaction intermediate and final products characterization. *Mat. Sci. Eng. A Struct.* **2007**, *465*, 199–210. [CrossRef]
60. Grapes, M.D.; Reeves, R.V.; Fezzaa, K.; Sun, T.; Densmore, J.M.; Sullivan, K.T. In situ observations of reacting Al/Fe_2O_3 thermite: Relating dynamic particle size to macroscopic burn time. *Combust. Flame* **2019**, *201*, 252–263. [CrossRef]
61. Shin, M.S.; Kim, J.K.; Kim, J.W.; Moraes, C.A.M.; Kim, H.S.; Koo, K.K. Reaction characteristics of Al/Fe_2O_3 nanocomposites. *J. Ind. Eng. Chem.* **2012**, *18*, 1768–1773. [CrossRef]
62. Monazam, E.R.; Breault, R.; Siriwardane, R. Reduction of hematite (Fe_2O_3) to wüstite (FeO) by carbon monoxide (CO) for chemical looping combustion. *Chem. Eng. J.* **2014**, *242*, 204–210. [CrossRef]
63. Montgomery, Y.C.; Focke, W.W.; Kelly, C. Measurement and modelling of pyrotechnic time delay burning rates: Application and prediction of a fast burning delay composition. *Propell. Explos. Pyrot.* **2017**, *42*, 1289–1295. [CrossRef]
64. Huang, S.; Deng, S.; Jiang, Y.; Zheng, X. Experimental effective metal oxides to enhance boron combustion. *Combust. Flame* **2019**, *205*, 278–285. [CrossRef]
65. Sullivan, K.; Young, G.; Zachariah, M.R. Enhanced reactivity of nano-B/Al/CuO MIC's. *Combust. Flame* **2009**, *156*, 302–309. [CrossRef]
66. Wainwright, E.R.; Dean, S.W.; Lakshman, S.V.; Weihs, T.P.; Gottfried, J.L. Evaluating compositional effects on the laser-induced combustion and shock velocities of Al/Zr-based composite fuels. *Combust. Flame* **2020**, *213*, 357–368. [CrossRef]